

Mapping spin-polarised transitions with atomic resolution

P. Schattschneider,^{1,2} B. Schaffer,^{3,4} I. Ennen,² and J. Verbeeck⁵

¹*Institut für Festkörperphysik, Technische Universität Wien, A-1040 WIEN, Austria*

²*University Service Centre for Electron Microscopy,
Technische Universität Wien, A-1040 WIEN, Austria*

³*SuperSTEM, STFC Daresbury Laboratories, Keckwick Lane, Warrington, WA4 4AD, UK*

⁴*Kelvin Nanocharacterisation Centre, SUPA School of Physics and Astronomy,
University of Glasgow, Glasgow, G12 8QQ, Scotland, UK*

⁵*EMAT, University of Antwerp, Groenenborgerlaan 171, 2020 Antwerp, Belgium*

A numerical analysis of the coupling between Angstrom-sized electron probes and spin polarised electronic transitions shows that the inelastically scattered probe is in a mixed state containing electron vortices with non-zero orbital angular momentum. These electrons create an asymmetric intensity distribution in energy filtered diffraction patterns, giving access to maps of the magnetic moments with atomic resolution. A feasibility experiment shows evidence of the predicted effect. Potential applications are column-by-column maps of magnetic ordering, and the creation of Angstrom-sized free electrons with orbital angular momentum by inelastic scattering in a thin ferromagnetic foil.

PACS numbers: 03.65.Vf (Phases, topological), 07.79.-v (scanning probe microscopes), 75.25.-j (spin arrangement), 78.20.Fm (dichroism), 82.80.Dx (analytical methods involving electron spectroscopy)

I. INTRODUCTION

With the availability of electron vortices of sub-nm scale in the transmission electron microscope (TEM) [1–3] and its theoretical description[4–6] many potential applications come within reach, ranging from the transfer of angular momentum to nanoparticles, over utilisation of the intrinsic magnetic moment of vortex electrons to the probing of chirality[7]. Indeed, chiral electronic transitions were the first application of electron vortices in energy loss magnetic chiral dichroism (EMCD) [1].

The discovery of EMCD [8] was an unexpected alternative to XMCD (X-ray magnetic circular dichroism) with the convenient side effect that additional information on the investigated material can be obtained simultaneously via standard analytical techniques[9, 10]. The spatial resolution of this electron microscopical technique is now in the nanometer range [11]. A modification of the technique has been shown to be site selective [12]. The excellent spatial resolution and the site selectivity are important for the study of novel materials such as Heusler alloys[13, 14], nanoparticles or interfaces [15]. Recent advances in electron microscopy have led to the imaging of condensed matter with subatomic resolution [16–18]. On this basis it has been speculated that the mapping of spin polarized electronic transitions - and thus the mapping of spin and orbital polarization - on the atomic scale could be feasible in a TEM, applying the EMCD technique[19]. An incident plane wave affecting a spin polarized L_{23} transition would break the mirror symmetry of non-magnetic transitions in the scattered wave. This symmetry breaking could be analysed either with asymmetric objective apertures or with a cylinder lens[20, 21]. However, for technical reasons both approaches are unrealistic in the TEM.

On second thoughts it becomes evident that the in-

elastic interaction of an incident electron with a spin polarized electronic transition creates a scattered electron with topological charge. One can thus apply the theory of vortex electrons[5] to the outgoing wave field. In a sense, this is a bottom-up application of the original idea of using incident vortex electrons for EMCD. The reason that this works is the generalized reciprocity theorem[22] that confirms the equivalence of the incident and the outgoing (also called reciprocal[23]) electron for inelastic scattering. This observation raises two questions: How can an EMCD signal be detected with Angstrom-sized Scanning TEM (STEM) probes; and can one produce electron vortices without holographic masks?

Here, we present a theoretical and numerical analysis of the coupling between an Angstrom-sized STEM probe and an atom-sized vortex field via a chiral electronic transition. It is shown that the inelastically scattered probe is in a mixed state containing electron vortices with non-zero angular momentum. These electrons create an asymmetric intensity distribution in energy filtered diffraction patterns, giving access to maps of the magnetic moments on an atomic column-by-column basis. A feasibility experiment shows evidence of the predicted effect. Finally 2 potential applications are discussed: maps of magnetic ordering with atomic resolution; and the creation of free electrons with orbital angular momentum and a diameter of about 0.1 nm by inelastic scattering in a thin ferromagnetic foil.

II. THEORY

We focus on the model of a thin (ideally one atom) layer of Fe. In this case the dynamical equation for the propagation of the probe's density matrix is considerably simplified. We give here only the basic equation for the

propagator and refer the reader to the relevant literature for details [19, 21, 24–26].

The inelastic intensity at energy loss E in the exit plane of the specimen is the diagonal term $\rho(\mathbf{r}, \mathbf{r})$ of the density matrix:

$$\rho_E(\mathbf{r}, \mathbf{r}) = \int \int \bar{G}_{d-z}(\mathbf{r}, \mathbf{x}) \bar{G}_{d-z}^*(\mathbf{r}', \mathbf{x}') T_E(\mathbf{x}, \mathbf{x}', z, z') \phi_z^*(\mathbf{x}) \phi_{z'}(\mathbf{x}') d^2x d^2x' e^{iq_e(z-z')} dz dz' \quad (1)$$

where z, z' are variables along the optical axis and \mathbf{r}, \mathbf{x} are in the plane perpendicular to the optical axis. G is the elastic propagator of electrons in the crystal. ϕ_z is the wave function of the incident electron at depth z and $q_E = k_o - k_i$ is the minimum wave number transfer in the inelastic interaction, equal to the difference between wave numbers of the outgoing and the incident electron.

The inelastic scattering kernel $T_E(\mathbf{x}, \mathbf{x}', z, z')$ is characteristic for the electronic transitions creating an energy loss E . For thin specimens and atomic columns without defects the z integration can be performed in closed form [27]. For spin polarized dipole transitions the atomic scattering kernel reads

$$T_E(\mathbf{x}, \mathbf{x}) = \sum_{\mu=-1}^1 |\psi_\mu(\mathbf{x})|^2 \sum_{s=\uparrow, \downarrow} C_{j\mu}^{\uparrow, \downarrow} n^{\uparrow, \downarrow}. \quad (2)$$

with

$$\psi_{\pm 1}(\mathbf{x}) = e^{\pm i\alpha} \frac{i}{2\pi} \int_0^\infty \frac{q^2 J_1(qx) \langle j_1(Q) \rangle_{ELSj}}{Q^3} dq \quad (3a)$$

$$\psi_0(\mathbf{x}) = \frac{qE}{2\pi} \int_0^\infty \frac{q J_0(qx) \langle j_1(Q) \rangle_{ELSj}}{Q^3} dq, \quad (3b)$$

with the matrix element of the spherical Bessel function

$$\langle j_1(Q) \rangle = \langle I | j_1(Q) | F \rangle$$

between initial and final target states. The coefficients $C_{j\mu}$ are weighting factors for spin-orbit coupling [21, 28, 29], and $n^{\uparrow, \downarrow}$ is the spin polarisation of the final state. The spin-orbit coupling of the initial state renders the coefficients C dependent on the total magnetic quantum number $j = l + s$. For the L_{23} edges to be considered $j = 1/2$ or $j = 3/2$. The essential property that we will focus on is described by Eq.3a: It represents the outgoing inelastically scattered wave as an electron vortex with topology $m = \pm 1$ in the form of a Hankel transform that is easily computable from atomic wave functions.

The propagation of focussed probes through a thin specimen has regained interest in the context of real space STEM [30]. Even for elastic scattering the problem of propagating a focussed probe - as we shall adopt in the following - through a thin specimen to the detector poses considerable numerical problems. The inelastic interaction that can take place throughout the specimen thickness adds another complexity. Therefore Eq.1 cannot

be solved without approximations, at least with present numerical capacity. We are obliged to restrict the discussion to a model system that allows to analyse the salient features of the inelastic coupling process with an accuracy comparable to the available experimental data [31]. As such we choose a line of equally spaced atoms with given spin polarisation; we shall calculate the contributions from each transition in dipole approximation, discuss the signal from a single atom and finally build a line profile of the energy filtered signal from the array of atoms. In the case of a line of atomic scattering centres the elastic propagators G in Eq.1 collapse into delta functions [32], and Eq. refrhoout2 reads

$$\rho_E(\mathbf{r}, \mathbf{r}') = T(\mathbf{r}, \mathbf{r}') \phi_0^*(\mathbf{r}) \phi_0(\mathbf{r}'). \quad (4)$$

Eq. 2 allows us to separate the problem into 3 terms: each transition channel $\mu \in [-1, 1]$ can be factorised into a product of wave functions, and we get for the outgoing intensity in channel μ

$$\rho_\mu(\mathbf{r}, \mathbf{r}) = \bar{C}_{j\mu} \varphi_\mu(\mathbf{r}) \varphi_\mu^*(\mathbf{r}) \quad (5)$$

with

$$\bar{C}_{j\mu} = \sum_{s=\uparrow, \downarrow} C_{j\mu}^{\uparrow, \downarrow} n^{\uparrow, \downarrow} \quad (6)$$

and

$$\varphi_\mu(\mathbf{r}) = \psi_\mu(\mathbf{r}) \phi_i^*(\mathbf{r}). \quad (7)$$

The intensity in the diffraction plane is calculated from the 2D-Fourier transform of Eq. 5:

$$\rho_\mu(\mathbf{q}, \mathbf{q}) = \bar{C}_{j\mu} |FT_{\mathbf{r}}[\varphi_\mu(\mathbf{r})]|^2 \quad (8)$$

as the trace over the 3 transitions channels μ :

$$\rho_E(\mathbf{q}, \mathbf{q}) = Tr_\mu[\rho_\mu(\mathbf{q}, \mathbf{q})] = \sum_\mu \rho_\mu(\mathbf{q}, \mathbf{q}). \quad (9)$$

The trace operator shows formally that the scattered electron cannot be described by a wave function because it is in a mixed state. With the coefficients C for L_{23} transitions we can compute the outgoing intensity and the corresponding diffraction patterns. Without loss of generality we assume complete spin polarisation for the final target states (as is justified for the L edges of the 3d ferromagnets that we will use as a demonstration example).

Let us focus on the L_3 edge: For complete spin polarisation the values for $\bar{C}_{j\mu}$ are given in Table I [21] The image intensity Eq.4 will then contain different contributions from the scattering channels for spin up and spin down polarisations. This difference is the basis of EMCD.

However, scrutinising Eq.5 for an incident plane wave, one notes that $|\varphi_\mu|^2 = |\varphi_{-\mu}|^2$ because the phase factors of both the incident plane wave and the kernel - $e^{\pm i\alpha}$ - cancel in the intensity. That means that there will be

j	1/2 (L_2)			3/2 (L_3)			
	μ	-1	0	1	-1	0	1
\uparrow		0.056	0.111	0.167	0.278	0.222	0.167
\downarrow		0.167	0.111	0.056	0.167	0.222	0.278
unpolarized		0.111	0.111	0.111	0.222	0.222	0.222

TABLE I. Prefactors $C_{j\mu}^{\uparrow,\downarrow}$. The first two rows are the weighting factors for the transitions when the final states are completely (up or down) spin polarized. The third row gives the weighting factors for unpolarized final states. (All per electron).

no difference in the image Eq.5 for spin up or for spin down polarisations. The same is true for the intensity in the diffraction plane Eq.9. Essentially, it is not possible to see spin polarisation from single atoms in the TEM without further action.[33]

The situation changes completely when using a STEM probe instead of a plane incident wave. We analyse the situation qualitatively before considering numerical simulations. We assume a narrow focussed probe given by the Airy function \mathcal{A} at a distance \mathbf{R} from the atom. (The diameter of the probe be smaller than R and so small that the amplitude of the kernel is almost constant within the probe. In the following numerical simulation this condition is relieved.) Then we can approximate the outgoing wave in channel μ as

$$\varphi_\mu(\mathbf{r}) = \psi_\mu(\mathbf{r} - \mathbf{R})\mathcal{A}(\mathbf{r}) \approx \mathcal{A}(\mathbf{r})|\psi_\mu(R)|e^{i\mu\alpha(\mathbf{r})}. \quad (10)$$

Note that the outgoing wave is more extended than the Airy disk because of the long range Coulomb coupling force; in Fig. 1, it is drawn not to scale (even larger for better visibility). The azimuth angle within the outgoing disk is $\alpha \doteq \alpha(\mathbf{R}) + \mu y/R$ in the coordinate system shown in Fig.1 and we see that the phase of the outgoing wave depends on the position of the STEM probe and changes sign when going from $\mu = 1$ to -1 . Via the shift theorem the diffraction pattern will be proportional to a shifted Fourier transform of the Airy function, i.a. a disk function $\Pi(\mathbf{q})$

$$\rho_\mu(\mathbf{q}, \mathbf{q}) = \bar{C}_{j\mu} |\psi_\mu(R)|^2 \Pi(\mathbf{q} + \mu \hat{\mathbf{q}}_y/R) \quad (11)$$

that is: the diffraction pattern is shifted by $-1/R, 0, 1/R$ in direction of the unit vector $\hat{\mathbf{q}}_y$ for the 3 transition channels. Having established an observable that has the signature of a particular transition channel the spin polarisation of a single atomic column can be determined.

III. NUMERICAL SIMULATIONS

First we construct the outgoing signal for each of the 3 transition channels, $\rho_\mu(\mathbf{r}, \mathbf{r})$, shown in Fig.2. These are L_3 energy filtered images of a STEM probe of 0.1 nm diameter scanning across a single atom. From top to bottom are the transition channels $\mu = -1, 0, +1$. From left to right the distance R to the atom is $-2, -1, 0, 1, 2$

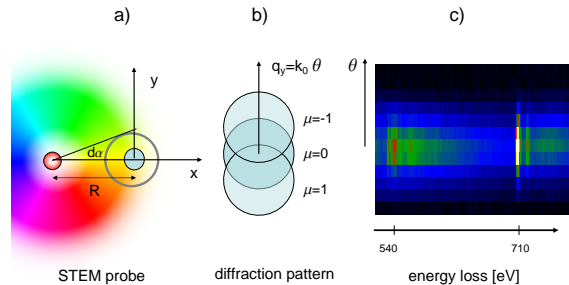


FIG. 1. Schematic of the principle of probe-vortex coupling. a) Top view of a narrow incident Airy disk (gray), focussed at a distance R in scan direction (x) from the atom (red). The scattering kernel T_E is symbolised as a diffuse cloud with a color coded phase, increasing from blue to red in clockwise rotation for the $\mu = 1$ channel. According to Eq.10, the outgoing wave (gray circle) has acquired a phase ramp $d\alpha = \mu y/R$ in the chiral transition. b) The phase ramp translates into a shift of the diffraction disk by μ/R in direction q_y . c) the q_x extension is squeezed into one pixel on the detector in the (q, E) geometry. Note that the energy loss axis must be perpendicular to q_y , which is proportional to the scattering angle, $q_y = k_0\theta$. The (θ, E) map is a true image taken on magnetite ranging from the oxygen K edge at ~ 540 eV to the Fe L_{23} edge at ~ 710 eV.

at.units. Note that the STEM probe is always in the center of the squares. The side structures at distances of $R = \pm 2$ at.u. are signals from the second maximum of the Airy disk that coincides here with the atom centre. Brightness codes intensity of the image, color codes for the phase of the wave function. When the Airy disk sits on the atom the outgoing beam is a true atomic vortex with topological charge $\mu \in [-1, 0, 1]$. At larger distance phase ramps in the Airy disks develop, visible as continuous color variations. They change sign when crossing the atom centre and are opposite for $\mu = \pm 1$. Each square has a side length of 5 at.units (0.26 nm).

These phase ramps are responsible for the corresponding shifts of the diffraction patterns shown in Fig.3. Color codes for the intensity in arbitrary units (blue: low, red: high). The shift of the patterns in vertical direction (q_y) is opposite for $\mu = \pm 1$ and depends on the position of the probe. The $\mu = 0$ channel does not show any shift because it lacks a phase ramp in the image.

Since the $\mu = \pm 1$ channels contribute differently for spin up/spin down polarisation via the coefficients $C_{j\mu}$, Eq.6, the diffraction patterns will be different for these two cases. (Note that this is not the case in the image: there, the difference is only in the phase, not in the intensity distribution).

Monitoring energy filtered diffraction patterns of a

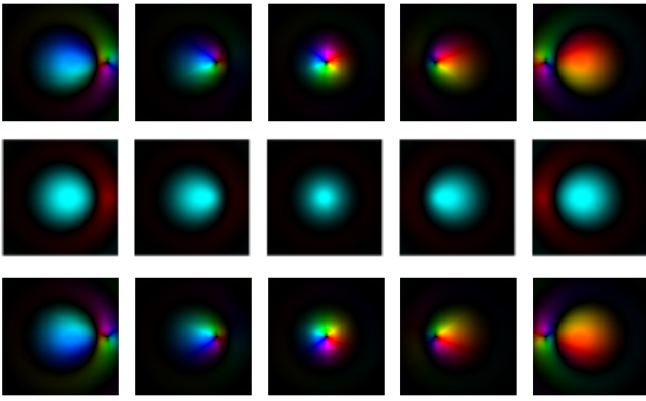


FIG. 2. Fe L_3 energy filtered real space exit wave functions φ_μ from Eq. 7 of a STEM probe of 0.1 nm diameter scanning across a single atom for the 3 dipole allowed transition channels. From top to bottom: transition channels $\mu = -1, 0, +1$. From left to right: distance R to the atom $-2, -1, 0, 1, 2$ at. units. Brightness codes intensity of the image, color codes for the phase of the wave function. When the Airy disk sits on the atom (center column) the outgoing beam is a real vortex with $\mu \in [-1, 0, 1]$. At a distance phase ramps in the Airy disks develop, changing sign with R and with μ . Each square has a side length of 5 at. units (0.26 nm).

scanned probe means measuring a multidimensional data cube because background subtraction and multiple scattering deconvolution of energy loss spectra require a range of losses. Such data has two dimensions (q_x, q_y) in the reciprocal space, one in the energy-loss (eV), and one (x) or two (x, y) in the real space, depending on the scanning pattern. This creates huge data files - a scan over 1 elementary cell in magnetite with 0.02 nm step width with 256^2 pixels in the diffraction pattern would give ~ 60 Mb per energy channel, approaching ~ 10 GB for a whole spectrum - and is impracticable. One can however exploit a remarkable feature apparent in the simulations: The diffraction patterns show only asymmetry with respect to the coordinate q_y , which is the Fourier transformed variable of y . An experimental setup could then discard the q_x variable by integration without losing information. This is exactly what is realised in the so-called (q, E) geometry, shown in Fig.1c. There, the q_x axis is squeezed onto one pixel of the spectrometer by compressive lenses whereas the q_y axis is retained, being projected on the detector perpendicular to the energy loss axis. This is sketched in Fig.1c: a (q_y, E) data set for a fixed position R . Selecting the L_3 white line from the whole (q_y, E, R) data, a reduced subset with axes (R, q_y) is obtained. The scan direction must be perpendicular to y in the coordinate system of Fig.1. Contrary to XMCD or EMCD, the new technique operates on a single white line only (the stronger L_3 line here). This is important because often the L_2 edge is too faint to obtain sensible results. (It should be noted that for the separation of spin and orbital moments both L_2 and L_3 edges are needed [34, 35].

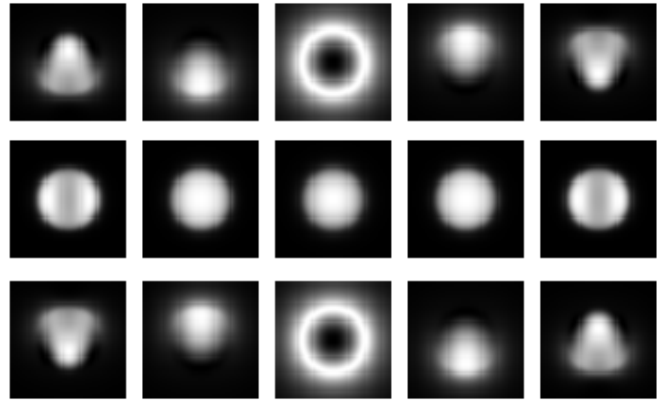


FIG. 3. Fe L_3 energy filtered diffraction patterns $\rho(\mathbf{q}, \mathbf{q})_\mu$ - Eq. 8 of a STEM probe of 0.1 nm diameter scanning across a single atom, corresponding to Fig.2. From top to bottom: transition channels $\mu = -1, 0, +1$. From left to right: distance R to the atom $-2, -1, 0, 1, 2$ at. units. Here, color codes for the intensity, in arbitrary units (blue: low, red: high). Note the shift of the patterns for $\mu = \pm 1$ in vertical direction q_y as predicted in Fig.1b, depending on the position of the probe, and the inversion of shifts with change of sign. The $\mu = 0$ channel does not show any shift because there is no phase ramp in the image. Simulation for 100 kV, convergence angle 18 mrad. The squares have a side length of ± 50 mrad.

These subsets can be constructed from the previous results, simply by integrating the intensity of Fig.3 over the "squeezed" variable q_x and summing over the 3 transition channels in Eq.9. The result is shown in Fig.4a for spin up and spin down configurations.

To enhance the asymmetry Fig.4a suggests to avoid the central part around $q_y = 0$ which adds only spin-insensitive intensity thus increasing the noise level. Integration of the density matrix Eq.8 over the scattering angle in the top and bottom parts yields two scans over a single atom

$$\begin{aligned} \rho_+(R) &= \int dq_x \int_{q_{y1}}^{q_{y2}} \rho(\mathbf{q}, \mathbf{q}) dq_y \\ \rho_-(R) &= \int dq_x \int_{-q_{y2}}^{-q_{y1}} \rho(\mathbf{q}, \mathbf{q}) dq_y \end{aligned} \quad (12)$$

where $q_y = k_0 \theta$. This is shown in Fig.4b for $\theta_{y1} = 20$ mrad, $\theta_{y2} = 50$ mrad. The difference between minimum and maximum is ~ 0.06 nm, indicating that Cs corrected machines and a high stability are needed to see the effect. Moreover, the signal will be very faint, such that noise would tend to override the possible effect. Dynamical diffraction of the incident and the outgoing electron on the lattice and remaining aberrations of the probe forming lens and the spectrometer will also complicate the situation. With present codes it is not possible to include these effects reliably in the simulation.

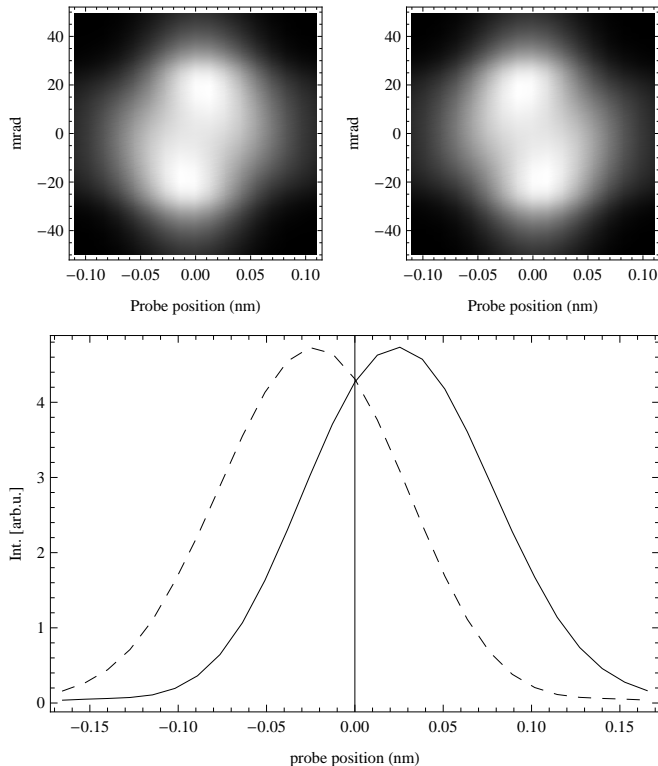


FIG. 4. Left: (R, q_y) signal distribution of a STEM probe of 0.1 nm diameter scanning across a single atom, corresponding to Fig.2. Left: spin up polarisation of the atom; right: spin down polarisation. The top/bottom asymmetry is well visible and can be used to determine the spin polarisation. Right: Top (full line) and bottom (dashed line) line scans of a STEM probe of 0.1 nm diameter across a single atom, corresponding to Fig.4a. Angular integration ranges -50 to -20 and 20 to 50 mrad.

IV. EXPERIMENTAL EVIDENCE

We have performed a feasibility experiment at the Daresbury SuperSTEM facility using a NION Ultra-STEM100 microscope[36]. The machine is a dedicated, aberration corrected STEM operated at 100 kV with a cold-FEG emitter. Its 3rd generation C3/C5 aberration corrector allow a typical probe size of 0.1 nm at a beam current of 30 pA. EELS spectrum imaging at atomic resolution is done with a DigiScan2 scanning unit in combination with an Gatan Enfina spectrometer. The difficulty of the experiment stems from the extreme demand on stability, the rather long dwell times causing beam damage in the Angstrom-sized spot, remaining aberrations, etc.

We investigated a platelet-like magnetite nanoparticle of ~ 15 nm diameter, Fig.5. The thickness in this region was between 5 and 10 nm, resembling as close as possible the single atomic row model. The STEM probe was scanned over a line of atoms as shown in fig.5 (green trace). Magnetite in (111) zone axis shows two types

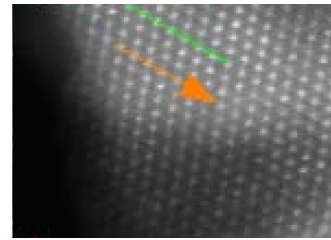


FIG. 5. HAADF image of the border of the magnetite nanoparticle in [111] zone axis orientation. The scan line is indicated in green, the axis of energy dispersion in orange is almost perfectly parallel to the scan direction, thus $q_y \parallel y$. The bright dots are the A columns containing 3 Fe atoms per unit cell in this projection. Their distance is 0.33 nm.

of Fe columns (hereafter called A and B), A containing 3 Fe atoms per elementary cell, B only one atom. The B columns are not visible in the HAADF image because of lower scattering strength and dynamical diffraction, confirmed by multislice simulations.

Fig. 6a shows the top and bottom profiles of the scan integrated from 20 to 50 mrad after standard background subtraction, drift correction and usual removal of the continuum signal beneath the white line[37]. A slight shift of the traces with respect to the atomic positions can already be surmised. However, the noise is almost overriding the signal.

In order to demonstrate the predicted effect qualitatively a Fourier analysis was performed on the two scans, retaining only coefficients up to lattice periodicity. The result is shown in Fig. 6b. The maxima are definitely shifted to both sides of the atom centres, marked by vertical lines. The average distance between the top and bottom scan maxima is 0.076 nm. One observes a rather large shift at the 0.33 nm position that is probably caused by some irregularity (noise, drift, etc). Excluding this value, the average difference is 0.65 nm. This is in good agreement with the simulational result of 0.6 nm, Fig.4b. Despite the crude approximations and the simple model the agreement is surprisingly good. More accurate models can be devised, but this is beyond the scope of the present paper as noise, drift and beam damage problems pose narrow limits on the interpretation of the data. More elaborate experiments with ultrathin magnetic specimens must be devised in order to confirm the present findings.

V. POTENTIAL APPLICATIONS

A. Detection of magnetic order

As described above and shown in Fig.4a, the top/bottom asymmetry in the (R, q_y) data set is caused by the spin polarisation on the atomic site. That provides a method for spin mapping. A straightforward way to do so is to take the first derivative of the difference

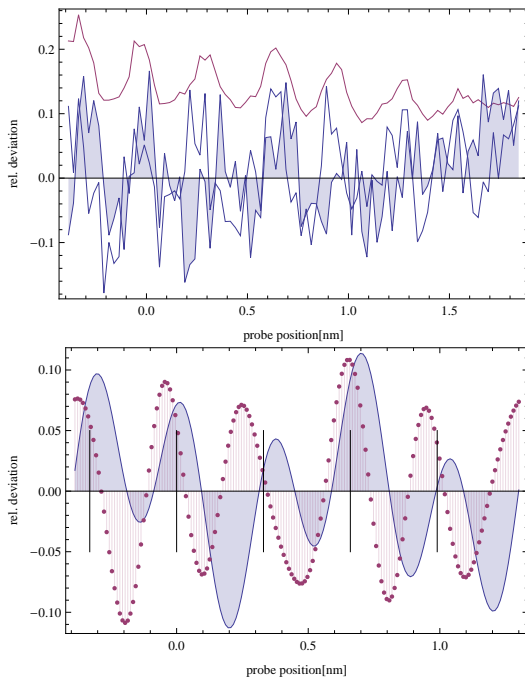


FIG. 6. Left: Top (filled curve) and bottom (empty curve) scans of the Fe L_3 white line signal after standard background subtraction, drift correction and removal of the continuum. The HAADF signal is superposed to show the positions of the A columns. The B columns are visible as a faint subsidiary peak. Right: Same scans after Fourier filtering. Positions of the MAADF maxima are marked with vertical lines.

(top-bottom) line scans ($\rho'_+ - \rho'_-$). Since the slope of the difference signal is strongest at the atomic sites, this scan gives directly the sign and position of the magnetic moment. Here we assume a hypothetical system with the same lattice constant as magnetite, also in (111) zone axis orientation, to make connection to real systems. Fig.7 shows the derivative $(\rho_+ - \rho_-)'(R)$ along a line scan as in Fig.5, for different assumptions of the magnetic ordering: Left for ferromagnetic, middle for antiferromagnetic, and right for ferrimagnetic ordering. To take account of the dechanneling and defocussing throughout the specimen the data was convolved with a 0.1 nm broadening function. The last panel resembles magnetite, in fact. In (111) zone axis projection the A columns contain 2 atoms spin up and on atom spin down, and the B columns contain one atom spin down, oriented in the magnetic field of the objective lens. On the other hand, the channeling is stronger on the deeper potential (A columns containing 3 atoms as compared to 1 on B) so the beam will see more from the A columns than from the B columns. This will weigh the A columns stronger than the B ones. The exact weighting factor is impossible to obtain without solving the dynamical equation for the propagator in the lattice, but a weighting coefficient between -50% and -25% for the B columns is reasonable. We chose -30%. Theoretically, it should be possible to perform such scans not only along lines but over areas. This should give atom-

resolved maps of the element specific magnetic moments and the magnetic ordering. But before establishing such an analytical technique many technical problems related to noise, stability, aberrations and dynamical diffraction must be solved.

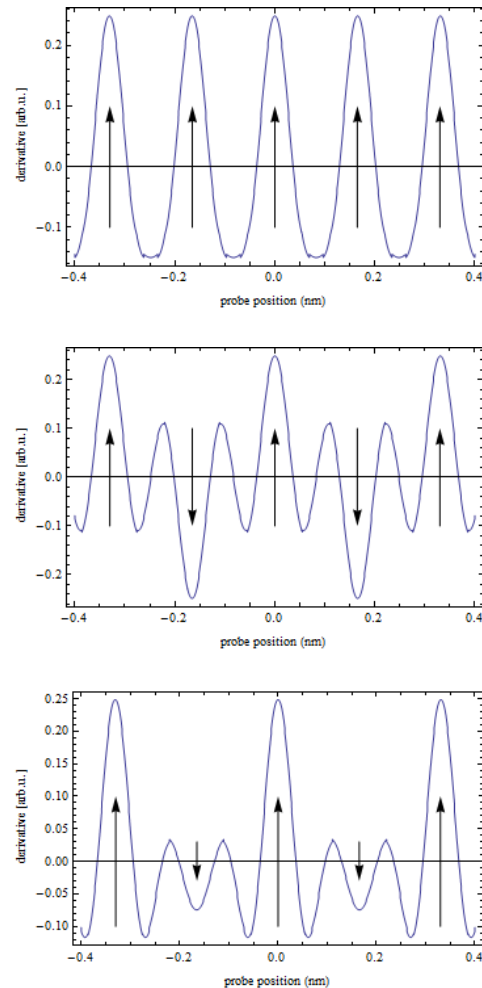


FIG. 7. Hypothetical line scan showing the first derivative $d(\rho_+(R) - \rho_-(R))/dr$ over an atomic row as in Fig. 5 for ferromagnetic (left), antiferromagnetic (middle) and ferrimagnetic ordering (right). The righermost panel was calculated with a relative strength of -30 % for the spin down moments.

B. Free electrons with angular momentum

A spot size of less than one Angstrom is feasible with C_s corrected microscopes. If such a beam is focussed exactly at the centre of an atom in a ferromagnet, say, the scattered electron has acquired orbital momentum. It is important to note that it is in a mixed state with contributions from the three transition channels $\mu \in [-1, 1]$, each creating a pure vortex state with topological charge μ . The expectation value of the angular momentum can

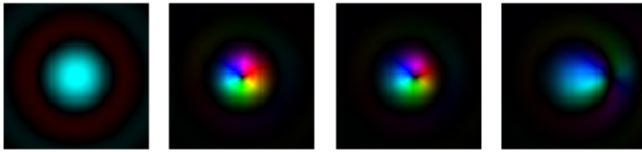


FIG. 8. The phase and amplitude of the incident Airy disk of 0.1 nm diameter (left) and for the scattered wave from the $\mu = 1$ transition. The atom is displaced from the beam center to the left by 0, 0.01, and 0.05 nm. The squares have a side length of 0.2 nm.

be calculated from the coefficients $C_{j\mu}$ given in Eq. 6:

$$\langle \mathcal{L}_z \rangle = \frac{Tr_\mu[\mathcal{L}_z \rho]}{Tr_\mu[\rho]} \in [-0.167\hbar, 0.167\hbar]$$

depending on the spin polarisation of the atom. This is a unique and simple method to create free electrons with orbital momentum, although the efficiency and the available momentum is probably too low to manipulate nanoparticles or even atoms by the torque. Another problem is the precise positioning of the probe on the atom. Fig. 8 shows the phase and amplitude of the incident beam of one Angstrom diameter and the scattered beam for the $\mu = 1$ transition when the atom is in the center, 0.01 nm, and 0.05 nm sideways. The vortex structure disappears rapidly, also visible in the intensity distribution Fig. 9. Here, the total electron density $Tr_\mu[\rho]$ is shown. The central dip, characteristic for the topological charge, remains at a deviation of 0.01 nm but has disappeared for 0.05 nm. Fig. 10a compares the incident Airy disk with the radial profile of the outgoing mixed state. The scattered state is even narrower than the Airy disk. The high sensitivity of the outgoing vortex state to the probe position could be used for a more direct method of spin mapping with sub-atomic resolution than described above, e.g. with a vortex filter such as a holographic mask.

We simulated also the scattered state when the incident beam is broader (0.5 nm diameter). The result is shown in Fig. 10b. The outgoing beam is broader than in case a) but still much narrower than the incident Airy disk, and is again a superposition of electron vortices. The not so surprising consequence is that a thin ferromagnetic foil in an electron beam creates free electrons carrying angular momentum after energy filtering [38]. This shows that vortices always have been there in EELS experiments on magnetic materials.

VI. CONCLUSION

The coupling of an Angstrom-sized electron probe to a spin polarised transition creates a mixed state that contains electron vortices with non-zero orbital momentum. These states break the symmetry of the scattering distribution in the far field in a way characteristic for the

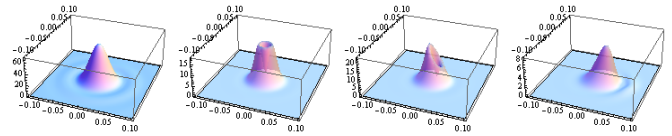


FIG. 9. Intensity of the incident Airy disk (left) and $Tr[\rho]$ for the scattered wave (mixed state from 3 transition channels) for atom displacements as in Fig. 8.

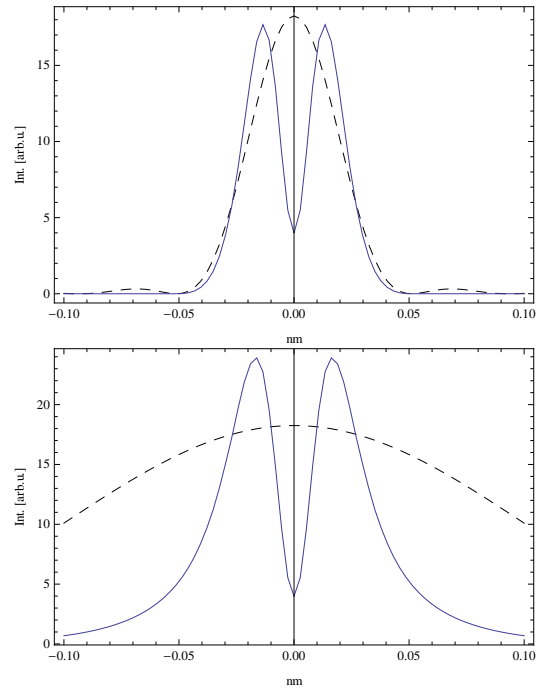


FIG. 10. a) Radial profiles of the incident one-Angstrom probe (dashed) and the outgoing electron density of the mixed state when the atom is exactly centred on the beam. b) The same for an incident probe of 5 Angstrom diameter.

chirality of the transition, a fact that can be used for the imaging of electron spins in real space with sub-Angstrom resolution.

A tentative experiment on a magnetite nanoparticle shows the expected asymmetry.

Apart from probing the local magnetic ordering, important for a number of technologically promising materials such as Heusler alloys, the proposed method can be used to map spin polarisations of single atomic columns, be that in the vicinity of interfaces, magnetically dead layers, or magnetic core-shell structures.

The creation of free electrons carrying angular momentum appears feasible, albeit with low efficiency, via spin polarised electronic transitions. This works even for relatively broad incident beams passing a thin ferromagnetic foil.

Acknowledgements: The authors thank Andrew Bleloch, Stefan Löffler and Peter Nellist for fruitful discussions and suggestions. P.S. acknowledges financial

support from the Austrian Science Fund, Project I543-N20. The support of the EPSRC for the SuperSTEM facility is gratefully acknowledged. J.V. acknowledges support from the European Research Council under the

7th Framework Program (FP7), ERC grant Nr. 246791 - COUNTATOMS and ERC Starting Grant 278510 - VORTEX.

-
- [1] J. Verbeeck, H. Tian, and P. Schattschneider, *Nature* **467**, 301 (2010).
- [2] J. Verbeeck *et al.*, *Applied Physics Letters* **99**, (2011).
- [3] S. Löffler and P. Schattschneider, submitted to *Ultramicroscopy* (2011).
- [4] K. Y. Bliokh, Y. P. Bliokh, S. Savel'Ev, and F. Nori, *Physical Review Letters* **99**, 190404 (2007).
- [5] P. Schattschneider and J. Verbeeck, *Ultramicroscopy* **111**, 1461 (2011).
- [6] K. Y. Bliokh, M. R. Dennis, and F. Nori, *Physical Review Letters* **107**, 174802 (2011).
- [7] H. L. Xin and D. A. Muller, *Nature Nanotechnology* **5**, 764 (2010).
- [8] P. Schattschneider *et al.*, *Nature* **441**, 486 (2006).
- [9] S. Rubino *et al.*, *Journal of Materials Research* **23**, 2582 (2008).
- [10] P. Schattschneider *et al.*, *Journal of Applied Physics* **103**, 07D931 (2008).
- [11] P. Schattschneider *et al.*, *Physical Review B - Condensed Matter and Materials Physics* **78**, 104413 (2008).
- [12] I. Ennen *et al.*, Submitted to *MMM* (2011).
- [13] S. Y. Yu *et al.*, *Appl. Phys. Lett.* **89**, 162503 (2006).
- [14] P. Shamberger and F. Ohuchi, *Phys. Rev. B* **79**, 144407 (2009).
- [15] R. F. Klie *et al.*, *Applied Physics Letters* **96**, 082510 (2010).
- [16] P. D. Nellist *et al.*, *Science* **305**, 1741 (2004).
- [17] O. L. Krivanek *et al.*, *Nature* **464**, 571 (2010).
- [18] D. A. Muller, *Nature Materials* **8**, 263 (2009).
- [19] *Linear and Chiral Dichroism in the Electron Microscope*, edited by P. Schattschneider (Pan Stanford Publishing, Singapore, 2011).
- [20] P. Schattschneider, J. Verbeeck, and A. L. Hamon, *Ultramicroscopy* **109**, 781 (2009).
- [21] P. Schattschneider *et al.*, *Physical Review B - Condensed Matter and Materials Physics* **82**, (2010).
- [22] S. D. Findlay, P. Schattschneider, and L. J. Allen, *Ultramicroscopy* **108**, 58 (2007), cited By (since 1996): 1.
- [23] Y. Kainuma, *Acta Cryst.* **8**, 247 (1955).
- [24] C. Dwyer, S. D. Findlay, and L. J. Allen, *Physical Review B* **77**, 184107 (2008).
- [25] P. Schattschneider, M. Nelhiebel, and B. Jouffrey, *Physical Review B - Condensed Matter and Materials Physics* **59**, 10959 (1999).
- [26] L. J. Allen and T. W. Josefsson, *Phys. Rev. B* **52**, 3184 (1995).
- [27] J. Verbeeck *et al.*, *Ultramicroscopy* **102**, 239 (2005).
- [28] B. T. Thole, P. Carra, F. Sette, and G. van der Laan, *Physical Review Letters* **68**, 1943 (1992).
- [29] J. Ruzs, S. Rubino, and P. Schattschneider, *Physical Review B* **75**, 214425 (2007).
- [30] J. Etheridge, S. Lazar, C. Dwyer, and G. A. Botton, *Physical Review Letters* **106**, (2011).
- [31] More involved model calculations such as multislice would not improve the results in view of the noisy data set.
- [32] This is also approximately true for specimens much thinner than the extinction length.
- [33] In the standard EMCD geometry, one uses the interference terms caused by Bragg scattering of the outgoing atomic vortices on the lattice, which is different for spin up and spin down polarisations.
- [34] J. Ruzs, O. Eriksson, P. Novák, and P. M. Oppeneer, *Physical Review B* **76**, 060408 (2007).
- [35] L. Calmels *et al.*, *Physical Review B* **76**, 060409(R) (2007).
- [36] O. L. Krivanek *et al.*, *Ultramicroscopy* **108**, 179 (2008).
- [37] The post-edge continuum, often used in standard EMCD for normalising, did not show periodic variations. Therefore it was not necessary to correct for, the more so as this would have induced additional noise.
- [38] The efficiency of this theoretical possibility is low in view of the low scattering cross section for the L edges.